

Ensembles of single-molecule picocavities as nonlinear optical metamaterials

Felipe Herrera^{1,2,*} and Marina Litinskaya^{3,†}

¹*Department of Physics, Universidad de Santiago de Chile, Av. Ecuador 3493, Santiago, Chile.*

²*ANID-Millennium Institute for Research in Optics, Chile.*

³*Department of Physics & Astronomy, University of British Columbia, Vancouver, Canada, V6T 1Z1*

(Dated: May 7, 2022)

Strong coupling with single molecules in plasmonic picocavities has emerged as a resource for room-temperature quantum control with nanoscale light. Tip-based nanoprobes can measure the local dynamics of individual molecular picocavities, but the overhead associated with sampling an inhomogeneous picocavity distribution can be challenging for scalability. We propose a macroscopic approach in which an ensemble of molecular picocavities acts as a nonlinear plasmonic metamaterial. Using a quantum optics perspective, we study theoretical performance limits for optical cross-phase modulation in the system, taking into account realistic distributions of picocavity volumes and molecular transition frequencies. The medium nonlinearity is mediated by local strong coupling with the lowest vibronic emission sideband of individual organic chromophores. The local vacua change the refractive index of the medium at the frequency of a weak probe field ω_p , set to drive the bare zero-phonon absorption band. Refractive index variations $\Delta n/n$ of a few percent, relative to a molecule-free scenario, are feasible with dilute ensembles. The probe phase evolution can be switched off in the presence of a signal field at a higher frequency ω_s , for intensities as low as 10 kW/cm^2 . The mechanism for optical switching involves a novel $(\omega_p + \omega_s)$ two-photon absorption channel, assisted by local vacuum fields. Our work paves the way for future studies of plasmonic metamaterials that exploit strong light-molecule interactions, for applications in optical state preparation and control.

I. INTRODUCTION

Organic chromophores in plasmonic picocavities [1–4], have emerged as promising platforms for studying cavity quantum electrodynamics (QED) at room temperature [5, 6]. Recent experiments [7] and rigorous theoretical modeling [8–11] have emphasized the quantum optical origin of commonly used plasmon-enhanced molecular spectroscopy techniques [12], offering new perspectives on conventional architectures that can stimulate the study of novel schemes for optical quantum control at the nanoscale [13].

Molecular cavity QED platforms based on optical microcavities, exploit the coupling of a cavity vacuum with collective vibronic coherences in an ensemble to reach the strong and ultrastrong coupling regimes [14–23]. The collective character of the interaction can enhance electric and charge transport processes [24–27], mediated by the cavity-induced delocalization of the molecular degrees of freedom involved in the transport process. Collective coupling can also lead to modifications of the chemical reactivity [28, 29] and optical response [30–33] of organic materials. Collectively strong coupling in microcavity occurs through a mechanism analogue to dipole synchronization [34]. However, the local field that each individual molecule experiences in a microcavity is very small.

In plasmonics, the extreme sub-wavelength field confinement achievable with current technology [35, 36] allows for light-matter interaction energies to overcome

local thermal fluctuations, at the level of individual molecules. This can enable the implementation of local control protocols that exploit strong vacuum fields to study optomechanical physics [7] and tailored photochemistry [37, 38]. Nanoparticle fabrication techniques can produce a large number of independent “molecular picocavities” [2]. The picocavity distribution can be strongly inhomogeneous, and must be sampled locally using tip-based nanoprobes [39–41], to extract spatially-resolved information about the light-matter coupling dynamics in the system. Although chemical methods are available to increase the homogeneity and reproducibility of the picocavity fabrication [4], the need to develop efficient local sampling method may be a challenge for the scalability and integrability of molecular picocavities in next-generation nanophotonic devices.

An alternative macroscopic approach was recently explored in Ref. [42]. It was shown that local light-matter coupling of individual molecules inside an optical microcavity can be exploited to imprint an effective optical nonlinearity on a molecular ensemble. The scheme involved the coupling of *cis-trans* molecular isomers (photoswitches) with the quantized field of a high-quality microcavity with a photon lifetime of several picoseconds. By exploiting the unique spectral and dynamical properties of molecular photoswitches and conditions of vacuum-induced transparency (VIT [43]), the feasibility of implementing cross-phase modulation using weak laser fields was demonstrated. The nonlinearity was shown to be robust with respect to static disorder in the molecular dipole orientation and molecular transition frequencies, under several constraints on the amount of vibrational and photonic decoherence in the system.

Building on Ref. [42], we propose a scheme for imple-

*Electronic address: felipe.herrera.u@usach.cl

†Electronic address: litinskaya@gmail.com

menting effective optical nonlinearities based on molecular strong coupling with a cavity field, without relying on VIT. We achieve this by relaxing key constraints imposed on the molecular and photonic variables, demonstrating that dilute ensembles of molecular picocavities can be directly used for nonlinear quantum optics, without the need to carry out local measurements of the intracavity fields. More specifically, we generalize the molecular species used in Ref. [42] to a broader class of organic chromophores that do not undergo photoisomerization. The only spectroscopic constraint imposed on the molecules is the resolution of a vibronic sideband in emission from the lowest excited singlet state $S_1 \rightarrow S_0$, at room temperature. On the photonic side, the only constraint is that the effective picocavity volumes should be small enough to enable the strong coupling regime locally with single molecules.

Starting with basic assumptions, now we demonstrate that strong coupling within individual molecular picocavities can be exploited to induce nonlinear phase modulation signals on a probe laser field that drives a disordered picocavity ensemble with a distribution of light-matter coupling strengths, natural inhomogeneous broadening of molecular transition frequencies, and sub-picosecond decoherence of molecular and photonic degrees of freedom. These are conditions that are currently found in experiments [1–4]. We derive theoretical bounds on the signal-to-noise ratio for nonlinear phase modulation on the probe field, and show that the predicted nonlinear observables are within experimental reach. Moreover, we demonstrate that the cavity-induced ensemble nonlinearity can be optically gated with a second control laser with an intensity as low as a few kW/cm^2 , i.e., orders of magnitude weaker than the light sources used in conventional nonlinear molecular spectroscopy [44].

In the rest of this article, we elaborate on the macroscopic approach that allows us to define the effective optical susceptibility of an ensemble of molecular picocavities (Sec. II) and a nonlinear phase modulation signal (Sec. III), then describe the quantum electrodynamics model that describes the light-matter dynamics within individual picocavities (Sec. IV), and finally study the dependence of the nonlinear phase modulation observables with the system parameters (Sec. V–VI). The main results of this work are summarized in Sec. VII.

II. EFFECTIVE MEDIUM APPROACH

Consider the plasmonic metamaterial in Fig. 1. It is composed of a thin dielectric layer with embedded plasmonic nanoparticle inclusions, randomly located in the dielectric. Inhomogeneous substrates of this type are commonly used in plasmon-enhanced spectroscopy [45–48]. The system contains a number of dimer structures with individual organic molecules embedded in their gap region, constituting an effective picocavity [1, 2]. In general, picocavities of varied geometries and material com-

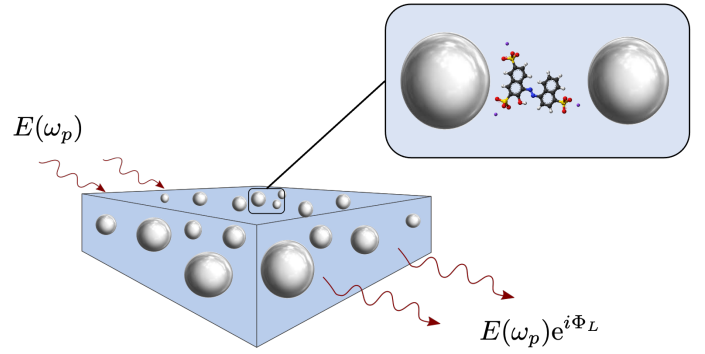


FIG. 1: **Plasmonic picocavity metasurface.** Large ensemble of metal nanoparticle inclusions on a thin dielectric layer subject to external in-plane driving by a probe field at frequency ω_p . Optical interactions with the ensemble results in a measurable phase shift Φ_L of the incoming wave. Nanoparticle structures can be engineered to support individual organic molecules inside gap regions of strong electromagnetic field confinement, implementing molecular picocavities (inset).

positions are characterized by extreme field confinement dimensions of sub-nanometer scales, in which strong coupling with individual molecules is possible [3, 4].

The optical response of the metamaterial can in principle be computed by solving Maxwell equations [49, 50]. For disordered picocavities with molecular dipoles in their field confinement region, the response must be averaged over an ensemble of disorder configurations. Large-scale numerical solvers can be used to construct the Green's function of the disordered metasurface [51, 52], from which evolution equations for the dynamics of the quantized molecular degrees of freedom can be formulated and solved using a macroscopic quantum electrodynamics framework [11, 53, 54].

In this work, instead of pursuing an exact calculation of the *absolute* response of the disordered picocavity ensemble, we are interested in estimating the *relative* contribution of the intracavity molecular degrees of freedom to the ensemble dynamics, a topic of recent interest in plasmonics [55]. In order to do this consistently, we adopt an effective medium perspective [56, 57], in which the ensemble of picocavities *without* molecules is treated as inclusions in a dielectric, and the local electric fields are averaged self-consistently to give a homogeneous effective dielectric constant ϵ_{eff} for the medium. The method is valid for inclusions that are isotropically distributed in the dielectric, with the typical size of the inclusions being much smaller than the relevant wavelengths. Effective medium theories have been successfully used to model the far field response of nanoparticle inclusions in bulk dielectrics [58], and thin films [59, 60]. Recent extensions have been developed to treat nanoparticle ensembles with strongly inhomogeneous field distributions [61], which are common in plasmonics.

We consider now the ensemble of embedded molecular dipoles, by decomposing the total polarization field into

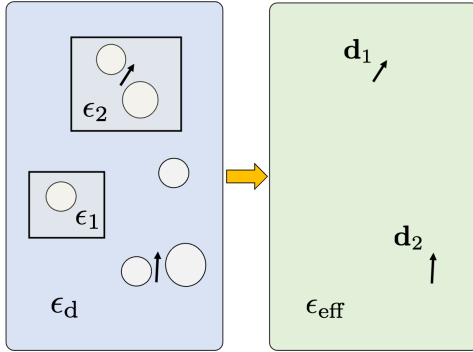


FIG. 2: **Effective medium example.** Nanoparticle inclusions with dielectric constants ϵ_1 (monomer) and ϵ_2 (dimer) are dispersed on a dielectric layer with dielectric constant ϵ_d (left panel). Dimer nanoparticles (picocavities) can host individual molecular dipoles within their volume. In the absence of molecules, the fields at the inclusions can be ensemble-averaged to give the dielectric constant ϵ_{eff} for the effective homogeneous medium. Molecular dipoles \mathbf{d}_i then act as a source for the macroscopic electric field in the medium (right panel).

three contributions: $\mathbf{P} = \mathbf{P}_d + \mathbf{P}_i + \mathbf{P}_m$, where \mathbf{P}_d corresponds to the pure dielectric matrix, \mathbf{P}_i is the contribution of the nanoparticle inclusions, and \mathbf{P}_m corresponds to the molecular dipoles. In an effective medium approach, the molecule-free background polarization $\mathbf{P}_{\text{bg}} = \mathbf{P} - \mathbf{P}_m$ and the corresponding local and macroscopic electric fields are averaged to give an effective dielectric constant of the form [57]

$$\frac{\epsilon_{\text{eff}} - \epsilon_d}{\epsilon_{\text{eff}} + 2\epsilon_d} = \sum_{i=1}^K \frac{N_i}{V} \alpha_i, \quad (1)$$

where α_i is the polarizability of the i -th type of inclusion, of which there are N_i in the dielectric volume V . $K = \sum_i N_i$ is the total number of inclusions in a background dielectric with dielectric constant ϵ_d . The density of inclusions is low enough to make dipolar interactions between inclusions negligible. Dilute ensembles with surface densities in the range $\sigma \sim 10 - 100 \mu\text{m}^{-2}$ can be prepared with inclusion sizes of few tens of nanometers [2, 45]. Using Eq. (1), ϵ_{eff} can in principle be computed, provided that the density, composition, and shapes of the K inclusions in the sample are known. Examples where this calculation procedure is carried out can be found in the literature [57].

In this framework, the molecular polarization $\mathbf{P}_m(t)$ is a source field for electromagnetic waves $\mathbf{E}(t)$ propagating in the effective homogeneous medium according to the wave equation

$$\left(\nabla^2 + \frac{\omega^2}{c^2} \epsilon_{\text{eff}}(\omega) \right) \mathbf{E}(\omega) = -\frac{\omega^2}{\epsilon_0 c^2} \mathbf{P}_m(\omega). \quad (2)$$

Self-consistency requires the molecular polarization to be linearly driven by the average field as $\mathbf{P}_m(\omega) =$

$\epsilon_0 \langle \chi(\omega) \rangle \mathbf{E}(\omega)$, where $\langle \chi(\omega) \rangle$ is the molecular susceptibility, averaged over the structural and energetic parameters that determine the coupling of molecular dipoles with the local field of the picocavity inclusions. In-plane propagation of a probe field $\mathbf{E}(\mathbf{r}_\parallel, t) = E_p \exp[i(\mathbf{k}_p \cdot \mathbf{r}_\parallel - \omega_p t)]$ is thus determined by the propagation constant $\beta_p = n(\omega_p) \omega_p / c$, where

$$n^2(\omega_p) = \epsilon_{\text{eff}}(\omega_p) [1 + \langle \chi(\omega_p) \rangle] \quad (3)$$

is the square of the effective refractive index at the probe frequency ω_p . In other words, provided that the assumptions of effective medium theory hold, we can transform the problem of wave propagation in a thin film with a dilute ensemble of molecular picocavities into an independent dipole problem in which $\epsilon_{\text{eff}}(\omega)$ and $\langle \chi(\omega) \rangle$ must be determined self-consistently, as illustrated in Fig. 2.

III. MOLECULE-INDUCED PHASE SHIFTS

General computational methods to simultaneously obtain $\epsilon_{\text{eff}}(\omega)$ and $\langle \chi(\omega) \rangle$, taking into account the quantized nature of the local fields \mathbf{E}_L inside the picocavity inclusions as well as the internal level structure of molecular dipoles, have yet to be developed [6]. Here, we simplify the discussion by assuming that the intracavity local fields and the probe wave are spectrally distinct. This allows us to estimate $\langle \chi(\omega_p) \rangle$ by separately averaging the quantized local fields of the picocavities, to give an induced molecular dipole moment at the probe frequency of the form $\mathbf{d}(\omega_p) = \langle \alpha(\omega_p) \rangle \mathbf{E}(\omega_p)$, where $\langle \alpha(\omega) \rangle$ is the average frequency-dependent polarizability of the molecular dipoles. For N molecules driven at ω_p , we thus have $\mathbf{P}_m(\omega_p) = N \mathbf{d}(\omega_p) / V$.

In general, the *absolute* response of the system to the probe field is dominated by ϵ_{eff} , since the polarizability of metal nanoparticles is much larger than those of molecules [62]. We thus expect that strong coupling within individual molecular picocavities to result in *variations* of the effective refractive index of the metamaterial, relative to its molecule-free value $n_{\text{eff}} \equiv \text{Re} \sqrt{\epsilon_{\text{eff}}}$. Detection of refractive index variations is a standard technique in plasmonic sensing [63].

We estimate the predicted molecule-induced refractive index variation $\Delta n/n$. Specifically, the phase shift accumulated by the probe field over the propagation distance L in the composite layer is $\Phi_L \equiv \text{Re} \{ n(\omega_p) \} \omega_p L / c$. Straightforward estimates of $\Delta n/n$ can be done for $\text{Im} \{ \epsilon_{\text{eff}} \} \rightarrow 0$ and $|\langle \chi \rangle| \ll 1$, giving $n/n_{\text{eff}} \approx 1 + \text{Re} \langle \chi \rangle / 2$. In the absence of molecules, $\langle \chi \rangle$ vanishes at all frequencies, and $\Phi_L = n_{\text{eff}} \omega_p L / c$. The presence of molecules in each picocavity perturbs the phase shift to Φ'_L , such that

$$\frac{\Phi'_L - \Phi_L}{\Phi_L} = \text{Re} \langle \chi(\omega_p) \rangle \propto \left(\frac{N}{V} \right) \frac{|d_{eg}|^2}{2\epsilon_0 \hbar} \quad (4)$$

where $|d_{eg}|^2$ is the dipole moment for the transition induced at the probe frequency. For typical transition

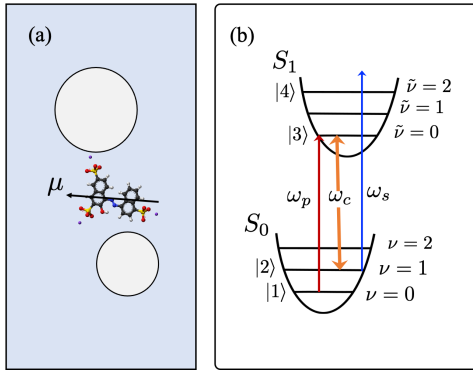


FIG. 3: **Light-matter coupling scheme:** (a) Illustration of a molecular transition dipole embedded in the gap volume of a dimer nanoparticle inclusion. (b) Displaced oscillator model for the ground (S_0) and first excited (S_1) singlet electronic states of an intracavity molecule. The cavity field drives a vibronic coherence between the $\nu = 1$ and $\tilde{\nu} = 2$ states at frequency ω_c . The zero-phonon line is driven by a weak laser probe at frequency ω_p , and a signal laser drives a hot-band vibronic coherence between $\nu = 1$ and $\tilde{\nu} = 2$, at frequency ω_s .

dipoles $d_{\text{eg}} \sim 1$ Debye (3.8 Debye in Ref. [4]), the magnitude of the relative phase is primarily limited by the number density of molecular picocavities. Large phase variations $(\Phi'_L - \Phi_L)/\Phi_L$ of a few percent can already be achieved with number densities $N/V \sim 10 \mu\text{m}^{-3}$, consistent with our dilute regime assumptions and experiments [4, 64]. Estimating the absolute phase shift Φ'_L , i.e., including intracavity molecules, would require knowledge of n_{eff} for a given inclusion configuration, which is beyond our scope in this work.

IV. INTRACAVITY LIGHT-MATTER COUPLING SCHEME

Optical phase variations induced by the intracavity molecules depend on the dynamics of the internal molecular coherences. We study this dynamics for molecules within the lowest electronic potentials S_0 and S_1 , as illustrated in Fig. 3b. The ground ($\nu = 0$) and first excited ($\nu = 1$) vibrational levels in S_0 are coupled to the lowest vibrational level ($\tilde{\nu} = 0$) in S_1 , by the probe and cavity fields, respectively. The Huang-Rhys factor [65] in S_1 is large enough to give a sizable oscillator strength for the $\nu = 0 \leftrightarrow \tilde{\nu} = 1$ vibronic sideband. The vibrational frequency ω_v is assumed to exceed $k_b T/\hbar$ at room temperature, as is typical with vinyl stretching modes ($\omega_v \approx 0.18$ eV) [35]. The picocavity frequency is set to $\omega_c = \omega_{00} - \omega_v$, with ω_{00} being the $0 \rightarrow 0$ vibronic absorption frequency. The large detuning from the ω_{00} peak prevents the cavity from driving population out of the ground vibrational state ($\nu = 0$) in the absence of the probe. Each picocavity thus only drives molecular coherences.

In addition to the probe field at frequency ω_p and the

picocavity field at ω_c , we introduce in Fig. 3b another classical *signal field* at frequency ω_s . The signal field drives the hot vibronic absorption band $\nu = 1 \rightarrow \tilde{\nu} = 2$ off-resonantly. We show later that this signal field can be used as an optical switch, for controlling the molecular susceptibility at the probe frequency. In summary, we have the frequency hierarchy $\omega_c < \omega_p < \omega_s$.

In order to compute $\langle \chi(\omega) \rangle$, we label the relevant vibrational and vibronic states of the molecule as $|1\rangle \equiv |\nu = 0\rangle$, $|2\rangle \equiv |\nu = 1\rangle$, $|3\rangle \equiv |\tilde{\nu} = 0\rangle$, and $|4\rangle \equiv |\tilde{\nu} = 2\rangle$, according to the scheme in Fig. 3b, to write a picocavity Hamiltonian of the form (we use $\hbar \equiv 1$ throughout)

$$\begin{aligned} \hat{\mathcal{H}} = & \omega_c \hat{a}^\dagger \hat{a} + \omega_{21} |2\rangle \langle 2| + \omega_{31} |3\rangle \langle 3| + \omega_{41} |4\rangle \langle 4| \\ & + g_c |3\rangle \langle 2| \hat{a} + \Omega_p |3\rangle \langle 1| e^{-i\omega_p t} + \Omega_s |4\rangle \langle 2| e^{-i\omega_s t} \\ & + \text{H.c.} \end{aligned} \quad (5)$$

where $\omega_{ij} = (E_i - E_j)/\hbar$ denote the molecular transition frequencies, g_c is the picocavity vacuum Rabi frequency, Ω_p is the classical Rabi frequency of the probe field, and Ω_s is the classical signal Rabi frequency. The bosonic cavity field operator is \hat{a} , and H.c. implies Hermitian conjugation. Energy is given relative to the ground vibrational level (i.e., $E_1 = 0$).

For a quantized picocavity in the low-excitation manifold, the molecular basis should be supplemented with Fock states $|n_{c_i}\rangle$, to give the dressed basis: $|\tilde{1}\rangle \equiv |1; 0_c\rangle$, $|\tilde{2}\rangle \equiv |2; 1_c\rangle$, $|\tilde{3}\rangle \equiv |3; 0_c\rangle$, and $|\tilde{4}\rangle \equiv |4; 1_c\rangle$. In the dressed-state picture, the probe field Ω_p drives the transition $|\tilde{1}\rangle \leftrightarrow |\tilde{3}\rangle$ within the vacuum manifold, and the signal field Ω_s drives the transition $|\tilde{2}\rangle \leftrightarrow |\tilde{4}\rangle$ within the one-photon manifold. The picocavity field admixes the vacuum and one-photon states $|\tilde{2}\rangle$ and $|\tilde{3}\rangle$.

We model the evolution of the reduced density matrix $\hat{\rho}(t)$ for an individual picocavity with a Lindblad quantum master equation of the form [42]

$$\frac{d}{dt} \hat{\rho} = -i[\hat{\mathcal{H}}, \hat{\rho}] + \sum_{\alpha} \hat{L}_{\alpha} \hat{\rho} \hat{L}_{\alpha}^\dagger - \frac{1}{2} (\hat{L}_{\alpha}^\dagger \hat{L}_{\alpha} \hat{\rho} + \hat{\rho} \hat{L}_{\alpha}^\dagger \hat{L}_{\alpha}), \quad (6)$$

where $\hat{\mathcal{H}}$ is given in Eq. (5), and \hat{L}_{α} is the Lindblad operator associated with the α -th dissipative channel. In Table I, we list the Lindblad operators used in this work, and the associated dephasing times in the bare basis. We use a notation in which the rate γ_{ij} describes the decay of the off-diagonal element $\rho_{ij} \equiv \langle i | \hat{\rho} | j \rangle$, in the dressed basis. For example, vibrational relaxation from $\nu = 1$ (state $|2\rangle$) to $\nu = 0$ (state $|1\rangle$) in S_0 occurs at the rate $\gamma_v \sim 1 \text{ ps}^{-1}$. On the other hand, the bare picocavity photon lifetime is $\kappa^{-1} \sim 10 - 100 \text{ fs}$ [35]. Therefore, the combined decay rate of the dressed Raman coherence $\langle \tilde{1} | \hat{\rho} | \tilde{2} \rangle$ is $\gamma_{21} = \gamma_v + \kappa$, as $|\tilde{2}\rangle$ has single-photon character. The lifetime of the excited electronic state S_1 is $\gamma_{31} \equiv \gamma_e$, given by either fluorescence or internal conversion. We set $\gamma_{41} \equiv \gamma_{31}$ throughout.

Dissipative Process	Lindblad operator (\hat{L}_α)	Timescales
Cavity photon leakage (κ)	$\sqrt{\kappa}\hat{a}$	$\sim 10 - 10^2$ fs
Intramolecular vibrational relaxation in S_0 (γ_v)	$\sqrt{\gamma_v} 1\rangle\langle 2 $	~ 1 ps
Intramolecular vibrational relaxation in S_1 (γ'_v)	$\sqrt{\gamma'_v} 3\rangle\langle 4 $	~ 1 ps
Dephasing of zero-phonon resonance (γ_e)	$\sqrt{\gamma_e} 1\rangle\langle 3 $	$\sim 1 - 10^3$ ps

TABLE I: Description and notation of the incoherent channels considered in this work (left), the associated Lindblad operators in the bare basis (center), and the corresponding decoherence timescales (right).

V. HOMOGENEOUS AUTLER-TOWNES RESPONSE

Starting from the master equation in Eq. (6), we follow Ref. [42] and derive a general expression for susceptibility

for a homogeneous ensemble of N independent molecules in identical single-molecule picocavities, subject to classical driving by the probe and signal fields. We obtain

$$\chi(\omega_p) = \left(\frac{N}{V}\right) \frac{|d_{13}|^2}{\epsilon_0\hbar} \times \frac{[\Delta_{21} + i\gamma_{21}][\Delta_{41} + i\gamma_{41}] - \Omega_s^2}{[\Delta_{31} + i\gamma_{31}]([\Delta_{21} + i\gamma_{21}][\Delta_{41} + i\gamma_{41}] - \Omega_s^2) - g_c^2[\Delta_{41} + i\gamma_{41}]}, \quad (7)$$

where $|d_{31}|^2$ is the 0-0 oscillator strength, $\Delta_{31} \equiv \omega_p - \omega_{31}$ is the probe detuning, $\Delta_{21} \equiv \omega_p - \omega_c - \omega_{21} = \Delta_{31} - \Delta_c$ is the two-photon Raman detuning. Introducing the cavity detuning $\Delta_c \equiv \omega_c - \omega_{32}$ and the signal detuning $\Delta_s \equiv \omega_s - \omega_{42}$, we can write $\Delta_{41} \equiv \Delta_{31} - \Delta_c + \Delta_s$.

The ensemble susceptibility in Eq. (7) involves only the single-molecule coupling strength g_c , highlighting the local character of the cavity-induced nonlinearity. This occurs because the cavity field drives a coherence between two states that are not populated ($|2\rangle$ and $|3\rangle$). This situation should be compared with the usual \sqrt{N} scaling of the Rabi coupling with molecular density [6]. In the notation of Eq. (4), we have $2\chi = (N/V)(|d_{13}|^2/\epsilon_0\hbar)\bar{\chi}$.

In Fig. 4, we plot the absorptive and dispersive parts of the disorder-free susceptibility $\chi(\omega_p)$ around the bare 0-0 absorption resonance, under conditions of strong intracavity coupling. In Fig. 4a, we show the system response without the signal field ($\Omega_s = 0$). The absorptive response shows two Autler-Townes (AT) peaks at $\omega_p \approx \omega_{31} \pm g_c$. The doublet opens a broad semi-transparent window (solid line), due to cavity-induced AT splitting of the dressed states $|\tilde{3}\rangle$ and $|\tilde{2}\rangle$. The width of the Autler-Townes transparency window Γ_{AT} can be defined by $A(\Gamma_{\text{AT}}/2) = A(g_c)/2$, with $A(\omega) \equiv \text{Im}\langle\chi(\omega)\rangle$. For a homogeneous system, Γ_{AT} scales linearly with the cavity coupling g_c [42]. On the other hand, the amount of residual absorption at the bare probe resonance ($\Delta_p = 0$), can be shown to scale with the ratio γ_{21}/γ_{31} [66].

Figure 4a shows that at the center of the AT doublet, the probe field experiences normal dispersion (dashed line), in contrast to the anomalous dispersion expected for an interference-based transparency window [66]. The

plot also shows a relatively broad region within the AT transparency window (order γ_{31} in frequency) in which probe dispersion overcomes absorption, i.e., $\text{Re}\chi(\omega_p) > \text{Im}\chi(\omega_p)$. Clearly this condition always holds away from absorptive resonances (e.g., $|\Delta_p| > 6$ in Fig. 4a). However, as we explain below, the ability of introducing a dispersive response in a frequency range that is otherwise opaque, is a key resource for optical switching.

In Fig. 4b, we show the susceptibility for the same conditions as in Fig. 4a, but now in the presence of a strong signal field ($\Omega_s = \gamma_{31}$), detuned from the $2 \rightarrow 4$ transition frequency ($\Delta_s = \gamma_{42}$). Up to a minor red shift of the peak AT_- , the probe response continues to exhibit the same AT doublet. However, now an absorption resonance destroys the transparency window when the multiphoton resonance condition $\Delta_p - \Delta_c + \Delta_s = 0$ holds. For $\Delta_c = 0$ and $\Delta_s = \gamma_{31}$, a power-broadened two-photon absorption resonance (TPA₄₁) occurs at $\Delta_p = -\gamma_{31}$. This TPA channel can be understood as a result of the mixing between the dressed states $|\tilde{2}\rangle$ and $|\tilde{3}\rangle$, mediated by an intracavity vacuum that acts as an effective doorway mechanism for the $(\omega_p + \omega_s)$ process

$$|1\rangle|0c\rangle \xrightarrow{\omega_p} (|3\rangle|0c\rangle \leftrightarrow |2\rangle|1c\rangle) \xrightarrow{\omega_s} |4\rangle|1c\rangle.$$

Note that the classical probe and signal fields do not change the intracavity photon number. This emerging TPA channel effectively modulates the dispersive response of the probe field within the AT window, by making absorption overcome dispersion (Fig. 4b, shaded area).

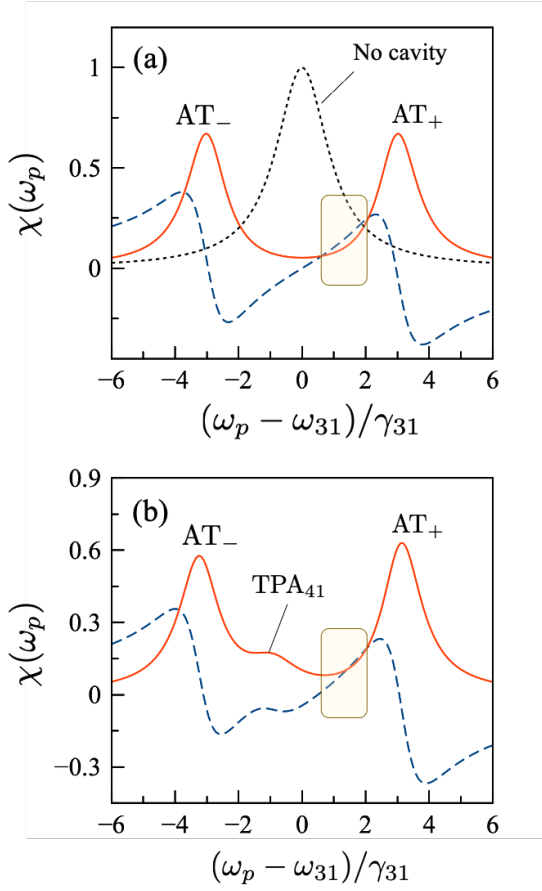


FIG. 4: **Disorder-free molecular susceptibility.** (a) Absorptive (solid line) and dispersive (dashed line) components of the homogeneous susceptibility $\chi(\omega_p)$ near the bare probe resonance (dotted line), in the absence of a signal field. The Autler-Townes (AT) doublet is shown. System parameters are $(g_c, \gamma_{21}, \gamma_{42}) = (3.0, 0.5, 1.0)$, in units of the homogeneous linewidth γ_{31} . (b) Absorptive and dispersive AT response with the same parameters as in panel (a), but in the presence of a signal field with Rabi frequency $\Omega_s = \gamma_{31}$, blue detuned by $\Delta_s = \gamma_{31}$ from the $2 \rightarrow 4$ transition. The AT doublet and a two-photon absorption (TPA₄₁) peak are shown. The shaded area shows a frequency region where dispersion overcomes absorption without the signal field, but in the presence of a signal field the relation inverts.

VI. DISORDER-AVERAGED AUTLER-TOWNES RESPONSE

A. Rabi and energy disorder

In this section, we study the lineshape of the AT transparency window under two types of structural disorder: random intracavity volumes disorder and random molecular transition frequencies. The first arises from the distribution of gap volumes V_g in the picocavity ensemble. The volume distribution is assumed to be Gaussian, with mean value $\langle V_g \rangle$ and standard deviation σ_{V_g} . Given that $g_c = f/\sqrt{V_g}$ [67], with f a constant, the distribution of

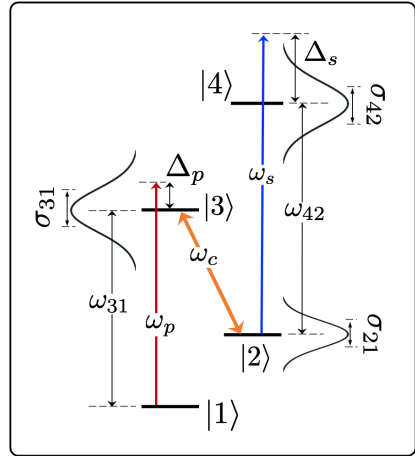


FIG. 5: **Inhomogeneous broadening scheme.** The probe absorption band at ω_{31} is inhomogeneously broadened due to static energy disorder by σ_{31} (FWHM $\approx 2.355\sigma_{31}$). The ground state vibrational band at ω_{21} is broadened by σ_{21} , and the inhomogeneous width of the hot-band absorption band is σ_{42} . The probe and signal fields are detuned from the peak frequencies by Δ_p and Δ_s , respectively. The ρ_{32} vibronic coherence is driven by an ensemble of cavity fields at ω_c , leading to a Gaussian distribution of Rabi frequencies with standard deviation σ_{g_c} .

Rabi frequencies g_c is also a Gaussian with mean value $\langle g_c \rangle = f/\sqrt{\langle V_g \rangle}$ and variance $\sigma_{g_c}^2 = f^2\sigma_{V_g}/2\langle V_g \rangle^{3/2}$.

In Fig. 5, we illustrate the Gaussian energy disorder of vibronic and vibrational transition frequencies. The inhomogeneous width of the cavity-free probe absorption band is σ_{31} (FWHM $\approx 2.355\sigma_{31}$). The ground state vibrational band $\nu = 0 \rightarrow \nu = 1$ has inhomogeneous width σ_{21} , and width of the hot-band absorption $\nu = 1 \rightarrow \tilde{\nu} = 2$ is σ_{42} . Since pure vibrational linewidths ($\sigma \sim 4$ meV [68]) are much smaller than typical vibronic linewidths ($\sigma \sim 100$ meV [65]), we have $\sigma_{21}/\sigma_{31} \ll 1$ and $\sigma_{42} \approx \sigma_{31}$.

In Fig. 6a, we plot the AT absorption doublet for an ensemble with a Gaussian distribution of Rabi frequencies, but otherwise homogeneous, in the absence of a signal field ($\Omega_s = 0$). In comparison with the fully homogeneous response from the previous section, the doublet lineshape remains largely unaltered even for broad distributions with $\sigma_{g_c} \approx \langle g_c \rangle$. This is reminiscent of the weak dependence of the cavity response on the distribution of dipole moment orientations found in Ref. [42].

In Fig. 6b, the AT lineshape is shown for an essentially homogeneous Rabi frequency distribution ($\sigma_{g_c} \rightarrow 0$), but the molecular levels are inhomogeneously broadened. No signal field is applied. The overall doublet shape of the AT transparency window is insensitive to the increase of the vibronic linewidths σ_{31} and σ_{42} . This is expected, as the AT transparency window is sustained by the cavity-induced Raman coherence $\rho_{21} = \langle 1, 0_c | \hat{\rho} | 2, 1_c \rangle$, which is limited by the photon decay rate κ .

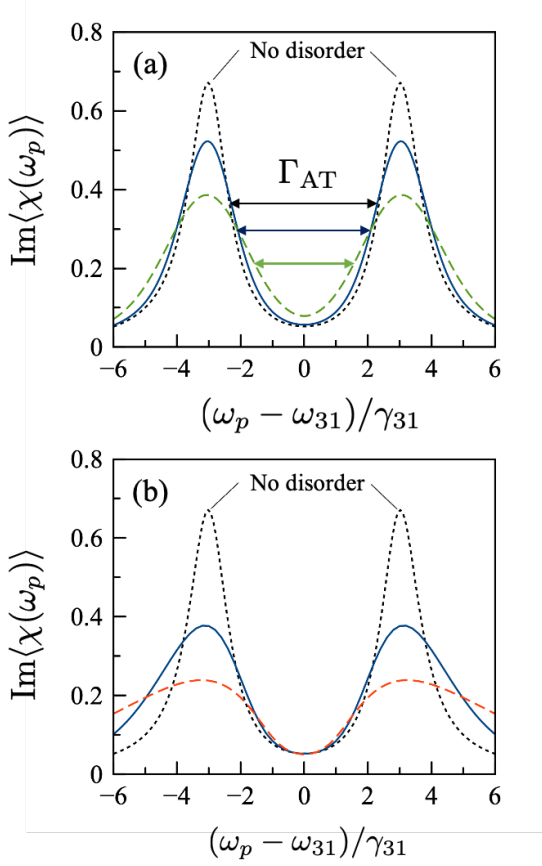


FIG. 6: **Autler-Townes doublet with inhomogeneous broadening.** (a) Probe absorption lineshape for a Gaussian distribution of Rabi couplings with mean value $\langle g_c \rangle = 3\gamma_{31}$, and variable standard deviation $\sigma_{g_c}/\gamma_{31} = 0$ (dotted line), 0.5 (solid line), and 1.0 (dashed line). No signal field is present and molecular transitions are homogeneously broadened, with $(\gamma_{21}, \gamma_{42}) = (0.5, 1.0)$, in units of γ_{31} . The Autler-Townes width Γ_{AT} is highlighted. (b) Absorption lineshape for a narrow Rabi frequency distribution with $(\langle g_c \rangle, \sigma_{g_c}) = (3.0, 0.01)$, in units of γ_{31} , and inhomogeneously broadened molecular levels with $\sigma_{31}/\gamma_{31} = 0$ (dotted line), 2.0 (solid line), and 4.0 (dashed line). In both panels, we set $\Delta_c = 0$.

B. Signal-to-noise ratio for phase modulation

We now study the feasibility of implementing the proposed optical switch in disordered picocavity ensembles. In order for the relative phase shift $\Delta\Phi_L/\Phi_L$ in Eq. (4) to be detectable in principle, dispersion of the probe field should overcome absorptive losses. Therefore, the signal-to-noise ratio, defined as

$$\eta_p(\omega_p) \equiv \frac{\text{Re}\chi(\omega_p)}{\text{Im}\chi(\omega_p)}, \quad (8)$$

must exceed unity over a frequency range $\Delta\omega_p \sim \gamma_{31}$. In a heterodyne setting that detects the interference of a transmitted probe field $E_p(\omega_p)$ with a phase reference, the ratio η_p correlates with the fringe visibility. If the

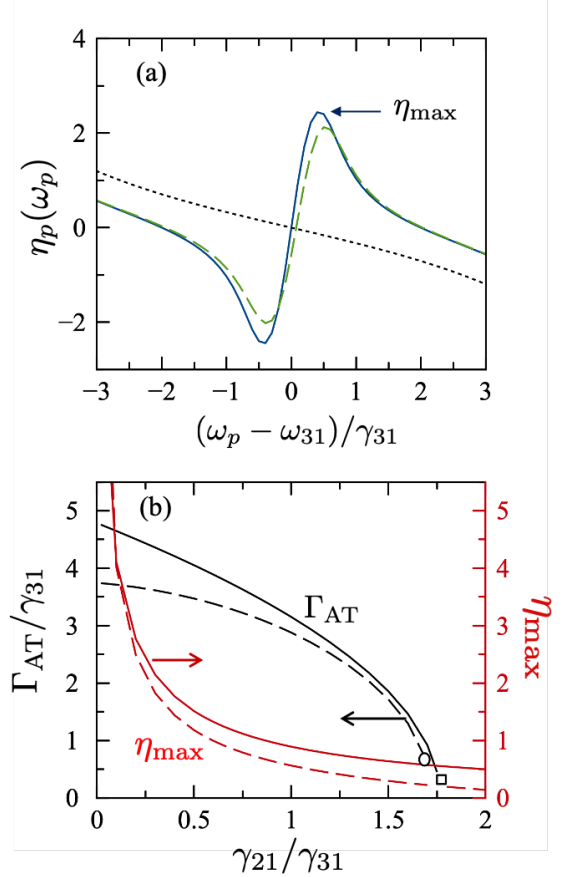


FIG. 7: **Autler-Townes transparency in a disordered ensemble.** (a) Signal-to-noise ratio η_p for refractive index variation within an Autler-Townes window with system parameters $(g_c, \sigma_{31}, \sigma_{21}) = (2.0, 2.0, 0.01)$, in units of γ_{31} . Curves are shown in the absence of the signal field (solid line), and in the presence of a signal field with $\Omega_s = 0.6\gamma_{31}$ and $\Delta_s = 1\gamma_{31}$ (dashed line). The maximum signal-to-noise ratio η_{max} is highlighted. Cavity-free results for the same broadening parameters are also shown (dotted line). (b) Left axis shows the Autler-Townes transparency width Γ_{AT} as a function of γ_{21} , for Lorentzian disorder (solid line) and Gaussian disorder (dashed line), with system parameters $(g_c, \sigma_{31}, \sigma_{21}, \Omega_s) = (3.0, 2.0, 0.01, 0)$, in units of γ_{31} . The right axis shows the corresponding optimal signal-to-noise ratio η_{max} for Lorentzian disorder (solid line) and Gaussian disorder (dashed line).

transmitted probe field is largely attenuated ($\eta_p \ll 1$), interference with a reference field cannot be resolved.

To account for energy disorder, we average Eq. (8) numerically using independent Gaussian distributions for each molecular transition frequency. We also analytically estimate this average using independent Lorentzian distributions. As we prove in Appendix A, this Lorentzian averaging reduces to replacing γ_{ij} in Eq. (7) with $\Sigma_{ij} = \gamma_{ij} + \sigma_{ij}$ everywhere. The analytical results allow us to gain insight into the multiple parameters that determine the effective nonlinear probe response. As shown below, we numerically confirm that a realistic Gaussian

disorder gives the same trends for key observables as the Lorentzian disorder model.

Using the Lorentzian disorder technique developed in Ref. [42], and described in Appendix A, it can be shown that in the absence of a signal field, the ratio η_p as a function of probe detuning Δ_p can be written for a resonant cavity ($\Delta_c = 0$) as

$$\eta_p(\Delta_p) = \frac{g_c^2 \Delta_p - \Delta_p(\Delta_p^2 + \Sigma_{21}^2)}{\Sigma_{31}(\Delta_p^2 + \Sigma_{21}^2) + \Sigma_{21}g_c^2}, \quad (9)$$

where the parameters $\Sigma_{ij} \equiv \gamma_{ij} + \sigma_{ij}$ represent total decoherence rates, including homogeneous (γ_{ij}) and inhomogeneous (σ_{ij}) contributions. In a cavity-free scenario, Eq. (9) reduces to the linear scaling $\eta_p = -\Delta_p/\Sigma_{31}$, shown in Fig. 7a for Gaussian disorder. The cavity vacuum induces a deviation from the linear scaling, such that an optimal ratio η_{\max} is reached when the probe is slightly detuned from the center of the AT window by

$$\Delta_p(\eta_{\max}) \approx g_c \sqrt{\frac{\Sigma_{21}}{\Sigma_{31} + 3\Sigma_{21}}}. \quad (10)$$

We drop quadratic terms in Σ_{21}/g_c . For low-quality picocavities in strong coupling, we have $\gamma_v \ll \kappa \lesssim \gamma_{31} < g_c$.

For the system parameters used in Fig. 7a, the Lorentzian disorder model predicts an optimal signal-to-noise ratio $\eta_{\max} \approx 2.0$ at $\Delta_p = 0.55 \gamma_{31}$. This detuning is only slightly higher than the value $0.41 \gamma_{31}$, predicted by numerically averaging over Gaussian disorder (Fig. 7a, solid line). In the presence of a signal field ($\Omega_s > 0$), blue detuned from the 4-2 resonance by $\Delta_s = \gamma_{13}$, the AT window lineshape becomes distorted (see Fig. 4), and η_{\max} decreases monotonically with increasing Ω_s (Fig. 7a, dashed line), as discussed in more detail below.

More generally, the optimal signal-to-noise ratio η_{\max} can be estimated in the Lorentzian disorder model as

$$\eta_{\max} = \frac{g_c}{\sqrt{\Sigma_{21}(\Sigma_{31} + 3\Sigma_{21})}} \left(\frac{\Sigma_{31} + 2\Sigma_{21}}{2\Sigma_{31} + 3\Sigma_{21}} \right), \quad (11)$$

where we have ignored terms that are second order in Σ_{21}/g_c . η_{\max} can be made large by having small Σ_{21} , as in Ref. [42]. Consider now an ensemble of lossy picocavities with a large Raman decoherence rate $\Sigma_{21} \sim \Sigma_{31}$. Equation (11) then predicts that cavity-mediated optical phase modulation within the AT transmission window can still be feasible, provided that the single-molecule Rabi coupling is strong enough. For example, we can achieve $\eta_{\max} \geq 1$ for $\Sigma_{21}/\Sigma_{31} = 1$, with Rabi couplings $g_c/\Sigma_{31} \geq 3.33$. For a representative zero-phonon linewidth $\Sigma_{31} \approx 50$ meV [4, 12], this corresponds to $g_c \approx 167$ meV. Improving the quality factor of the picocavities ($\Sigma_{21} \sim \kappa$), such that the ratio Σ_{21}/Σ_{31} decreases by a factor of two, reduces the constraint on single-molecule coupling to $g_c \geq 98$ meV, for phase modulation to be detectable. Single-molecule couplings of these magnitudes are within experimental reach [1, 3, 4, 69].

Complementary to the frequency-dependent signal-to-noise ratio $\eta_p(\omega_p)$, we can use the Lorentz disorder model

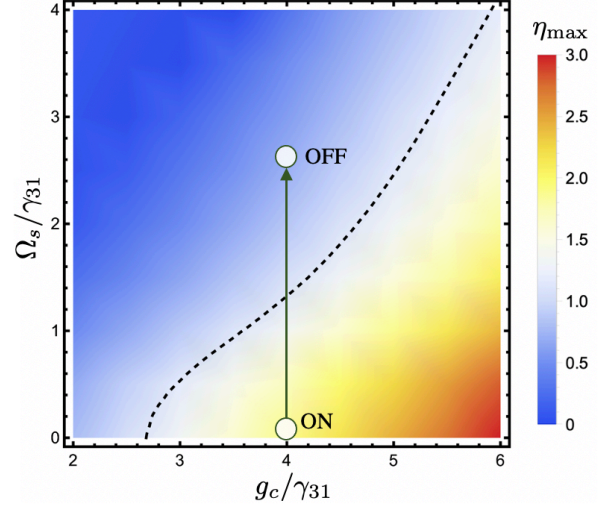


FIG. 8: **Signal-to-noise ratio for optical phase switching.** Optimal signal-to-noise ratio η_{\max} as a function of the cavity coupling strength g_c and signal strength Ω_s , in an Autler-Townes window corresponding to $(\sigma_{31}, \gamma_{21}, \sigma_{21}, \Delta_s) = (2.0, 0.5, 0.01, 1.0)$, in units of γ_{31} . The dashed contour marks the detection limit $\eta_{\max} = 1$, and two possible ON-OFF phase switch configurations are highlighted.

to analyze the lineshape of the Autler-Townes window. As already mentioned, the position of the AT_{\pm} doublet peaks is largely insensitive to disorder. However, transparency within the AT window is reduced as the quality of the vibrational Raman coherence ρ_{21} degrades with increasing γ_{21} and σ_{21} , which decreases the width Γ_{AT} .

In the Lorentz disorder model, the AT width can be written as

$$\Gamma_{\text{AT}} \approx 2\sqrt{g_c^2 - \sqrt{2}g_c(\Sigma_{31} + \Sigma_{21})}, \quad (12)$$

which shows that the AT window is formally closed when $g_c \leq \sqrt{2}(\Sigma_{21} + \Sigma_{31})$.

Figure 7 shows that the Lorentz disorder model in general overestimates Γ_{AT} relative to Gaussian averaging. For the parameters in Fig. 7b, the AT window is predicted by Eq. (12) to close for $\gamma_{21} = 1.78 \gamma_{31}$, which agrees well with the value ($1.71 \gamma_{31}$) obtained for Gaussian disorder. Figure 7b also shows that Eq. (11) correctly captures the scaling of η_{\max} with the Raman decay rate γ_{21} , for narrow vibrational coherences with $\sigma_{21} \ll \sigma_{31}$.

Finally, we study the dependence of η_{\max} on the signal field strength Ω_s , by numerically integrating Eq. (7) over independent Gaussian distributions for $(\omega_{31}, \omega_{21}, \omega_{42})$. As discussed above (see Fig. 4b), driving the picocavity ensemble with a strong blue-detuned signal field, effectively switches off optical phase modulation at the probe frequency, by introducing the two-color nonlinear absorption channel $(\omega_p + \omega_s)$, mediated by the picocavity vacuum.

In presence of the signal field, the signal-to-noise ratio (8) is to be calculated from real and imaginary parts

of $\chi(\omega_p)$ (7), averaged over independent fluctuations of molecular transitions ω_{31}, ω_{32} and ω_{42} . We find that the resulting signal-to-noise ratio can only be smaller than its $\Omega_s = 0$ value. Hence, Eq.(9) represents the upper bound for η_p .

Using Lorentz averaging technique, we found an analytical expression for $\chi(\omega_p)$ in [42]. We showed that the presence of the signal can be captured by a single dimensionless parameter,

$$\lambda_s = \frac{\Omega_s^2}{(\Delta_s^2 + \Sigma_{41}^2)}.$$

When λ_s is small, the signal-to-noise ratio is close to its Autler-Townes value in Eq. 9, and reaching $\eta_p > 1$ is feasible. For example, the dashed line in Fig. 7a corresponds to $\lambda_s = 0.036$, and the impact of the signal on the absorptive losses is indeed negligible. The requirement of smallness of λ_s can be understood as follows: The presence of the signal increases losses, since the signal beam is not protected by the AT transparency window. Making λ_s smaller effectively decouples the signal beam from the light-matter dynamics, either by reducing its strength or by increasing its detuning.

In Fig. 8, we show a parameter map $(g_c, \Omega_s, \eta_{\max})$ for optical switching with a signal field detuned by $\Delta_s = 1.0 \gamma_{31}$. We assume a relatively large Raman decay rate $\gamma_{21} = 0.5 \gamma_{31}$, to highlight the feasibility of the optical switching scheme under realistic picocavity conditions. For a typical S_1 radiative lifetime $1/\gamma_{31} \sim 1$ ns and inhomogeneous width $\sigma_{31} \sim 50$ meV, Fig. 8 shows that signal pulses with far-field intensities $I_s \sim 10$ kW/cm² ($d_{42} \sim 1$ D), are sufficient to switch off coherent phase modulation, in an ensemble of resonant picocavities in the Autler-Townes regime ($g_c > \Sigma_{31}$). These field intensities are orders of magnitude smaller than the typical two-photon excitation intensities used in photochemistry ($\sim 10^6$ W/cm² [70, 71]) or microscopy ($I \sim 10^{15}$ W/cm² [72, 73]).

VII. CONCLUSIONS

We propose and analyze ensembles of single-molecule plasmonic picocavities as effective nonlinear metamateri-

als, for light-by-light switching with low-intensity fields. We exploit the strong resonant coupling of the confined picocavity vacuum field at frequency ω_c , with excited vibrational levels in the ground and excited molecular potentials, S_0 and S_1 . Key to the proposed scheme is that the states that couple to picocavity field are not populated, i.e., the external fields do not create intracavity photons. This should be contrasted with the conventional linear and nonlinear microcavity spectroscopy, where external probes fields create photon population [17, 18, 74].

In our proposed scheme, molecular population is weakly removed from the ground state by a probe field at frequency $\omega_p < \omega_c$, resulting in an absorptive and dispersive response characteristic of an Autler-Townes doublet [66], around the bare zero-phonon (0-0) absorption resonance. We show that even for realistic ensembles with random cavity volumes, molecular energy disorder, and short-lived vibronic coherences, strong coupling inside the picocavities can induce sizable phase shifts $\Delta\Phi$ on the probe field, relative to a molecule-free scenario, suitable for detection using current nanoprobe heterodyne techniques [41].

Finally, we demonstrate that the coherent phase shifts on the probe field can be dynamically modulated by an additional signal field at frequency $\omega_s > \omega_p$, which is set to drive an excited state molecular coherence. The switching mechanism is identified as the opening of a novel two-color two-photon absorption process in the molecules at $\omega_p + \omega_s$, mediated and enhanced by the ensemble of picocavity vacua. For realistic system parameters, signal fields as weak as 10 kW/cm² are estimated to be sufficient for implementing optical switching behavior in a disordered picocavity ensemble. Our work thus opens the way toward the development of few-photon nonlinear optical devices with molecular picocavity metamaterials.

VIII. ACKNOWLEDGMENTS

F.H. is funded by ANID – Fondecyt Regular 1181743 and Millennium Science Initiative Program ICN17_012.

[1] Felix Benz, Mikolaj K. Schmidt, Alexander Dreismann, Rohit Chikkaraddy, Yao Zhang, Angela Demetriadou, Cloudy Carnegie, Hamid Ohadi, Bart de Nijs, Ruben Esteban, Javier Aizpurua, and Jeremy J. Baumberg. Single-molecule optomechanics in picocavities. *Science*, 354(6313):726–729, 2016.

[2] Cloudy Carnegie, Jack Griffiths, Bart de Nijs, Charlie Readman, Rohit Chikkaraddy, William M. Deacon, Yao Zhang, István Szabó, Edina Rosta, Javier Aizpurua, and Jeremy J. Baumberg. Room-temperature optical picocavities below 1 nm³ accessing single-atom geometries. *The Journal of Physical Chemistry Letters*, 9(24):7146–7151, 2018.

[3] Rohit Chikkaraddy, Bart de Nijs, Felix Benz, Steven J. Barrow, Oren A. Scherman, Edina Rosta, Angela Demetriadou, Peter Fox, Ortwin Hess, and Jeremy J. Baumberg. Single-molecule strong coupling at room temperature in plasmonic nanocavities. *Nature*, 535(7610):127–130, 07 2016.

[4] Rohit Chikkaraddy, V. A. Turek, Nuttawut Kongsuwan,

Felix Benz, Cloudy Carnegie, Tim van de Goor, Bart de Nijs, Angela Demetriadou, Ortwin Hess, Ulrich F. Keyser, and Jeremy J. Baumberg. Mapping nanoscale hotspots with single-molecule emitters assembled into plasmonic nanocavities using dna origami. *Nano Letters*, 18(1):405–411, 2018. PMID: 29166033.

[5] Thomas W Ebbesen. Hybrid Light-Matter States in a Molecular and Material Science Perspective. *Accounts of Chemical Research*, 49:2403–2412, 2016.

[6] Felipe Herrera and Jeffrey Owrutsky. Molecular polaritons for controlling chemistry with quantum optics. *The Journal of Chemical Physics*, 152(10):100902, 2020.

[7] Yuan Zhang, Ruben Esteban, Roberto A. Boto, Martin Urbieto, Xabier Arrieta, ChongXin Shan, Shuzhou Li, Jeremy J. Baumberg, and Javier Aizpurua. Addressing molecular optomechanical effects in nanocavity-enhanced raman scattering beyond the single plasmonic mode. *Nanoscale*, 13:1938–1954, 2021.

[8] A Delga, J Feist, J Bravo-Abad, and F J Garcia-Vidal. Theory of strong coupling between quantum emitters and localized surface plasmons. *Journal of Optics*, 16(11):114018, 2014.

[9] Tomáš Neuman and Javier Aizpurua. Origin of the asymmetric light emission from molecular exciton–polaritons. *Optica*, 5(10):1247–1255, Oct 2018.

[10] Tomáš Neuman, Javier Aizpurua, and Ruben Esteban. Quantum theory of surface-enhanced resonant raman scattering (serrs) of molecules in strongly coupled plasmon–exciton systems. *Nanophotonics*, 9(2):295–308, 2020.

[11] Johannes Feist, Antonio I. Fernández-Domínguez, and Francisco J. García-Vidal. Macroscopic qed for quantum nanophotonics: emitter-centered modes as a minimal basis for multiemitter problems. *Nanophotonics*, 10(1):477–489, 2021.

[12] Thomas Schmid, Lothar Opilik, Carolin Blum, and Renato Zenobi. Nanoscale chemical imaging using tip-enhanced raman spectroscopy: A critical review. *Angewandte Chemie - International Edition*, 52(23):5940–5954, 2013.

[13] M. S. Tame, K. R. McEnery, Ş. K. Özdemir, J. Lee, S. a. Maier, and M. S. Kim. Quantum plasmonics. *Nature Physics*, 9(6):329–340, jun 2013.

[14] V.M. Agranovich and G.C. La Rocca. Electronic excitations in organic microcavities with strong light–matter coupling. *Solid State Communications*, 135(9–10):544 – 553, 2005. Fundamental Optical and Quantum Effects in Condensed Matter.

[15] J. R. Tischler *et al.* Solid state cavity qed: Strong coupling in organic thin films. *Organic Electronics*, 8(2–3):94 – 113, 2007.

[16] S. Kéna-Cohen, M. Davanço, and S. R. Forrest. Strong exciton-photon coupling in an organic single crystal microcavity. *Phys. Rev. Lett.*, 101:116401, Sep 2008.

[17] Felipe Herrera and Frank C. Spano. Absorption and photoluminescence in organic cavity qed. *Phys. Rev. A*, 95:053867, May 2017.

[18] Felipe Herrera and Frank C. Spano. Dark vibronic polaritons and the spectroscopy of organic microcavities. *Phys. Rev. Lett.*, 118:223601, May 2017.

[19] M. Mazzeo *et al.* Ultrastrong light-matter coupling in electrically doped microcavity organic light emitting diodes. *Appl. Phys. Lett.*, 104(23), 2014.

[20] S. Gambino *et al.* Ultrastrong light-matter coupling in electroluminescent organic microcavities. *Applied Materials Today*, 1(1):33 – 36, 2015.

[21] T. Schwartz, J. A. Hutchison, C. Genet, and T. W. Ebbesen. Reversible switching of ultrastrong light-molecule coupling. *Phys. Rev. Lett.*, 106:196405, 2011.

[22] Stéphane Kéna-Cohen, Stefan A. Maier, and Donal D. C. Bradley. Ultrastrongly coupled exciton–polaritons in metal-clad organic semiconductor microcavities. *Advanced Optical Materials*, 1(11):827–833, 2013.

[23] P. A. Hobson, W. L. Barnes, D. G. Lidzey, G. A. Gehring, D. M. Whittaker, M. S. Skolnick, and S. Walker. Strong exciton–photon coupling in a low-Q all-metal mirror microcavity. *Applied Physics Letters*, 81(19):3519–3521, 2002.

[24] J. Feist and F. J. Garcia-Vidal. Extraordinary exciton conductance induced by strong coupling. *Phys. Rev. Lett.*, 114:196402, 2015.

[25] J. Schachenmayer, C. Genes, E. Tignone, and G. Pupillo. Cavity-enhanced transport of excitons. *Phys. Rev. Lett.*, 114:196403, 2015.

[26] Joel Yuen-Zhou, Semyon K Saikin, Tony Zhu, Mehmet C Onbasli, Caroline A Ross, Vladimir Bulovic, and Marc A Baldo. Plexciton dirac points and topological modes. *Nature Communications*, 7, 2016.

[27] David Hagenmüller, Johannes Schachenmayer, Stefan Schütz, Claudiu Genes, and Guido Pupillo. Cavity-enhanced transport of charge. *Phys. Rev. Lett.*, 119:223601, Nov 2017.

[28] James A Hutchison, Tal Schwartz, Cyriaque Genet, E. Devaux, and T. W. Ebbesen. Modifying Chemical Landscapes by Coupling to Vacuum Fields. *Angew. Chem. Int. Ed.*, 51(7):1592–1596, 2012.

[29] Felipe Herrera and Frank C. Spano. Cavity-controlled chemistry in molecular ensembles. *Phys. Rev. Lett.*, 116:238301, Jun 2016.

[30] F. Herrera *et al.* Quantum nonlinear optics with polar J-aggregates in microcavities. *J. Phys. Chem. Lett.*, 5(21):3708–3715, 2014.

[31] Fábio Barachati, Janos Simon, Yulia A. Getmanenko, Stephen Barlow, Seth R. Marder, and Stéphane Kéna-Cohen. Tunable third-harmonic generation from polaritons in the ultrastrong coupling regime. *ACS Photonics*, 5(1):119–125, 2018.

[32] Konstantinos S Daskalakis, Stefan A Maier, and Stéphane Kéna-Cohen. Polariton condensation in organic semiconductors. In *Quantum Plasmonics*, pages 151–163. Springer International Publishing, 2017.

[33] Giovanni Lerario, Antonio Fieramosca, Fábio Barachati, Dario Ballarini, Konstantinos S Daskalakis, Lorenzo Domenici, Milena De Giorgi, Stefan A Maier, Giuseppe Gigli, and Stéphane Kéna-Cohen. Room-temperature superfluidity in a polariton condensate. *Nature Physics*, 2017.

[34] B Zhu, J Schachenmayer, M Xu, F Herrera, J G Restrepo, M J Holland, and A M Rey. Synchronization of interacting quantum dipoles. *New Journal of Physics*, 17(8):083063, 2015.

[35] Denis G. Baranov, Martin Wersäll, Jorge Cuadra, Tomasz J. Antosiewicz, and Timur Shegai. Novel nanostructures and materials for strong light–matter interactions. *ACS Photonics*, 5:24–42, 2018.

[36] Eric A. Muller, Benjamin Pollard, Hans A. Bechtel, Ronen Adato, Dordaneh Etezadi, Hatice Altug, and

Markus B. Raschke. Nanoimaging and control of molecular vibrations through electromagnetically induced scattering reaching the strong coupling regime. *ACS Photonics*, 5(9):3594–3600, 09 2018.

[37] Simone Felicetti, Jacopo Fregoni, Thomas Schnappinger, Sebastian Reiter, Regina de Vivie-Riedle, and Johannes Feist. Photoprotecting uracil by coupling with lossy nanocavities. *The Journal of Physical Chemistry Letters*, 11(20):8810–8818, 2020.

[38] Jacopo Fregoni, Giovanni Granucci, Emanuele Coccia, Maurizio Persico, and Stefano Corni. Manipulating azobenzene photoisomerization through strong light-molecule coupling. *Nature communications*, 9(1):1–9, 2018.

[39] Nicolas Behr and Markus B. Raschke. Optical antenna properties of scanning probe tips. *The Journal of Physical Chemistry C*, 112(10):3766–3773, 03 2008.

[40] Molly A. May, David Fialkow, Tong Wu, Kyoung-Duck Park, Haixu Leng, Jaron A. Kropp, Theodosia Gougousi, Philippe Lalanne, Matthew Pelton, and Markus B. Raschke. Nano-cavity qed with tunable nano-tip interaction. *Advanced Quantum Technologies*, 3(2):1900087, 2020.

[41] Bernd Metzger, Eric Muller, Jun Nishida, Benjamin Pollard, Mario Hentschel, and Markus B. Raschke. Purcell-enhanced spontaneous emission of molecular vibrations. *Phys. Rev. Lett.*, 123:153001, Oct 2019.

[42] Marina Litinskaya and Felipe Herrera. Vacuum-enhanced optical nonlinearities with disordered molecular photo-switches. *Phys. Rev. B*, 99:041107, Jan 2019.

[43] J. E. Field. Vacuum-rabi-splitting-induced transparency. *Phys. Rev. A*, 47:5064–5067, Jun 1993.

[44] J D Bhawalkar, G S He, and P N Prasad. Nonlinear multiphoton processes in organic and polymeric materials. *Reports on Progress in Physics*, 59(9):1041, 1996.

[45] J. Britt Lassiter, Felicia McGuire, Jack J. Mock, Cristian Ciraci, Ryan T. Hill, Benjamin J. Wiley, Ashutosh Chilkoti, and David R. Smith. Plasmonic waveguide modes of film-coupled metallic nanocubes. *Nano Letters*, 13(12):5866–5872, 12 2013.

[46] Keiko Esashika, Ryo Ishii, Shunya Tokihiro, and Toshiharu Saiki. Simple and rapid method for homogeneous dimer formation of gold nanoparticles in a bulk suspension based on van der waals interactions between alkyl chains. *Opt. Mater. Express*, 9(4):1667–1677, Apr 2019.

[47] Pablo M. Jais, Daniel B. Murray, Roberto Merlin, and Andrea V. Bragas. Metal nanoparticle ensembles: Tunable laser pulses distinguish monomer from dimer vibrations. *Nano Letters*, 11(9):3685–3689, 09 2011.

[48] D Babonneau, D K Diop, L Simonot, B Lamongie, N Blanc, N Boudet, F Vocanson, and N Destouches. Real-time investigations of structural and optical changes in photochromic ag/TiO₂ nanocomposite thin films under laser irradiation. *Nano Futures*, 2(1):015002, feb 2018.

[49] K. L. Kelly, A. A. Lazarides, and G. C. Schatz. Computational electromagnetics of metal nanoparticles and their aggregates. *Computing in Science Engineering*, 3(4):67–73, 2001.

[50] Anuj Dhawan, Stephen J Norton, Michael D Gerhold, and Tuan Vo-Dinh. Comparison of fdtd numerical computations and analytical multipole expansion method for plasmonics-active nanosphere dimers. *Optics express*, 17(12):9688–9703, 2009.

[51] M. G. Araújo, J. M. Taboada, J. Rivero, D. M. Solís, and F. Obelleiro. Solution of large-scale plasmonic problems with the multilevel fast multipole algorithm. *Opt. Lett.*, 37(3):416–418, Feb 2012.

[52] Stéphanie Buil, Julien Laverdant, Bruno Berini, Pierre Maso, Jean-Pierre Hermier, and Xavier Quélin. Fdtd simulations of localization and enhancements on fractal plasmonics nanostructures. *Opt. Express*, 20(11):11968–11975, May 2012.

[53] Ludwig Knöll, Stefan Scheel, and Dirk-Gunnar Welsch. Qed in dispersing and absorbing media. In Jan Perina, editor, *Coherence and Statistics of Photons and Atoms*, Wiley Series in Lasers and Applications. Wiley-VCH, 2001.

[54] Christian Raabe, Stefan Scheel, and Dirk-Gunnar Welsch. Unified approach to qed in arbitrary linear media. *Phys. Rev. A*, 75:053813, May 2007.

[55] Maxim Sukharev and Abraham Nitzan. Optics of exciton-plasmon nanomaterials. *Journal of Physics: Condensed Matter*, 29(44):443003, oct 2017.

[56] Ari Sihvola. *Electromagnetic Mixing Formulas and Applications*. Electromagnetic Waves. Institution of Engineering and Technology, 1999.

[57] Vadim A. Markel. Introduction to the maxwell garnett approximation: tutorial. *J. Opt. Soc. Am. A*, 33(7):1244–1256, Jul 2016.

[58] Isabel Pastoriza-Santos, Daniel Gomez, Jorge Pérez-Juste, Luis M. Liz-Marzán, and Paul Mulvaney. Optical properties of metal nanoparticle coated silica spheres: a simple effective medium approach. *Phys. Chem. Chem. Phys.*, 6:5056–5060, 2004.

[59] Serge Berthier. Anisotropic effective medium theories. *J. Phys. I France*, 4(2):303–318, 1994.

[60] Yann Battie, Aotmane En Naciri, William Chamorro, and David Horwat. Generalized effective medium theory to extract the optical properties of two-dimensional nonspherical metallic nanoparticle layers. *The Journal of Physical Chemistry C*, 118(9):4899–4905, 03 2014.

[61] Krzysztof M. Czajkowski, Dominika Świtlik, Christoph Langhammer, and Tomasz J. Antosiewicz. Effective optical properties of inhomogeneously distributed nanoobjects in strong field gradients of nanoplasmmonic sensors. *Plasmonics*, 13(6):2423–2434, 2018.

[62] P. Törmä and W. L. Barnes. Strong coupling between surface plasmon polaritons and emitters: a review. *Rep. Prog. Phys.*, 78(1):013901, 2015.

[63] Yi Xu, Ping Bai, Xiaodong Zhou, Yuriy Akimov, Ching Eng Png, Lay-Kee Ang, Wolfgang Knoll, and Lin Wu. Optical refractive index sensors with plasmonic and photonic structures: Promising and inconvenient truth. *Advanced Optical Materials*, 7(9):1801433, 2019.

[64] Maria Papaioannou, Eric Plum, João Valente, Edward TF Rogers, and Nikolay I Zheludev. Two-dimensional control of light with light on metasurfaces. *Light: Science & Applications*, 5(4):e16070–e16070, 2016.

[65] Frank C Spano and Hajime Yamagata. Vibronic coupling in J-aggregates and beyond: a direct means of determining the exciton coherence length from the photoluminescence spectrum. *The journal of physical chemistry. B*, 115(18):5133–43, may 2011.

[66] M. Fleischhauer, A. Imamoglu, and J. P. Marangos. Electromagnetically Induced Transparency: Optics in Coherent Media. *Rev. Mod. Phys.*, 77:633–673, Jul 2005.

[67] Stefan A Maier. Plasmonic field enhancement and sers in the effective mode volume picture. *Optics Express*, 14(5):1957–1964, 2006.

[68] Benjamin Pollard, Eric A. Muller, Karsten Hinrichs, and Markus B. Raschke. Vibrational nano-spectroscopic imaging correlating structure with intermolecular coupling and dynamics. *Nature Communications*, 5(1):3587, 2014.

[69] Daqing Wang, Hrishikesh Kelkar, Diego Martin-Cano, Tobias Utikal, Stephan Götzinger, and Vahid Sandoghdar. Coherent Coupling of a Single Molecule to a Scanning Fabry-Perot Microcavity. *Physical Review X*, 7(2):021014, apr 2017.

[70] Yoichi Kobayashi, Katsuya Mutoh, and Jiro Abe. Step-wise two-photon absorption processes utilizing photochromic reactions. *Journal of Photochemistry and Photobiology C: Photochemistry Reviews*, 34:2–28, 2018.

[71] Mariacristina Rumi and Joseph W. Perry. Two-photon absorption: an overview of measurements and principles. *Adv. Opt. Photon.*, 2(4):451–518, Dec 2010.

[72] Karel Svoboda and Ryohei Yasuda. Principles of two-photon excitation microscopy and its applications to neuroscience. *Neuron*, 50(6):823–839, 2006.

[73] Gregor Langer, Klaus-Dieter Bouchal, Hubert Grün, Peter Burgholzer, and Thomas Berer. Two-photon absorption-induced photoacoustic imaging of rhodamine b dyed polyethylene spheres using a femtosecond laser. *Opt. Express*, 21(19):22410–22422, Sep 2013.

[74] Bo Xiang, Raphael F. Ribeiro, Yingmin Li, Adam D. Dunkelberger, Blake B. Simpkins, Joel Yuen-Zhou, and Wei Xiong. Manipulating optical nonlinearities of molecular polaritons by delocalization. *Science Advances*, 5(9), 2019.

Appendix A: Averaging over Energy Disorder: The Lorentzian Technique

Assume that the energies of states $|1\rangle, |2\rangle, |3\rangle$ and $|4\rangle$ fluctuate as a result of structural disorder (random environment). Then the detunings $\Delta_{31} = \omega_p - \omega_3 + \omega_1$ and $\Delta_{21} = \omega_p - \omega_c - \omega_2 + \omega_1$ also become random quantities. To find the disorder-averaged response, we can numerically integrate Eq. (7) in the main text. However, here will explore another route. Instead of using a realistic Gaussian distribution for molecular levels, we average the susceptibility over a *Lorentzian* distribution of the transition frequencies

$$P_L(x) = \frac{1}{\pi} \frac{\sigma_x}{(x - \langle x \rangle)^2 + \sigma_x^2}, \quad (\text{A1})$$

where $\langle x \rangle$ and σ_x are the mean value and the standard deviation of the random variable x . The benefit of this approach is that we will get exact analytical averages, which will allow us to gain insight into the system dynamics in simple terms, and help us make meaningful choices of parameters. We show numerically that the results of this procedure compare well with a Gaussian average (see Fig. 7b in the main text).

The proposed technique is based on the observation that there is a class of functions, for which averaging over a Lorentzian distribution can be done instantly. Consider a function of a complex variable $f(z = \Delta + i\gamma)$, where Δ and γ are real quantities; in what follows they will represent, respectively, a random detuning and a homogeneous linewidth. We assume that the function $f(z)$ satisfies two criteria: (1) it decays faster than z for $|z| \rightarrow \infty$, and (2) it does not have poles in the upper half-plane. Then averaging of $f(z)$ over a Lorentzian distribution (A1) $P_L(\Delta)$ of the detunings with the mean value $\langle \Delta \rangle$ and a standard deviation σ writes:

$$\begin{aligned} \langle f(\Delta + i\gamma) \rangle_{\Delta} &= \int_{-\infty}^{\infty} d\Delta f(\Delta + i\gamma) \frac{1}{\pi} \frac{\sigma}{(\Delta - \langle \Delta \rangle)^2 + \sigma^2} = \\ &= \int_{-\infty}^{\infty} d\Delta f(\Delta + i\gamma) \frac{1}{2\pi i} \left[\frac{1}{\Delta - (\langle \Delta \rangle + i\sigma)} - \frac{1}{\Delta - (\langle \Delta \rangle - i\sigma)} \right]. \end{aligned} \quad (\text{A2})$$

We can calculate this integral by closing the integration contour through the upper half-plane. By assumption (1) the integral over the half-circle vanishes, and by assumption (2) the function $f(z)$ has no poles inside the chosen integration contour, so that the only pole that contributes to the integral is $\Delta = \langle \Delta \rangle + i\sigma$ originating from the Lorentzian distribution in the first of the two integrals. By calculating the residue at this pole and applying the Cauchy theorem, we get:

$$\langle f(\Delta + i\gamma) \rangle_{\Delta} = f\left(\langle \Delta \rangle + i[\gamma + \sigma]\right), \quad (\text{A3})$$

In summary, as long as the function $f(\Delta + i\gamma)$ satisfies the two criteria listed above, averaging over a Lorentzian distribution consists in replacing the fluctuating detuning by its average value, and the linewidth γ by a sum of the homogeneous and inhomogeneous broadenings, denoted as $\Sigma = \gamma + \sigma$. We now notice that any susceptibility must satisfy the criteria (1) and (2), since they are the same requirements that are imposed on the material functions which satisfy the Kramers-Kronig relations.

Hence, averaging any material transition over Lorentzian disorder can be done by the replacement (A3). In our multi-level situation, we average the susceptibility over more than one Lorentzian distribution. To do this, we repeat this procedure subsequently for each of the disordered transitions. After averaging we get a new material function that satisfies the Kramers-Kronig relations and hence the criteria (1) and (2), so that we can keep repeating this procedure until all the averaging are completed. The result can be symbolically written as (here $\Sigma_i = \gamma_i + \sigma_i$):

$$\langle \chi(\Delta_1 + i\gamma_1, \dots, \Delta_N + i\gamma_N) \rangle_{\Delta_1, \dots, \Delta_N} = \chi\left(\langle \Delta_1 \rangle + i\Sigma_1, \dots, \langle \Delta_N \rangle + i\Sigma_N\right). \quad (\text{A4})$$
